

Research Article

Injection Molding Simulation of Polyoxymethylene Using Crystallization Kinetics Data and Comparison with the Experimental Process

Theresia Schrank ¹, Michael Berer ¹, Bernd Haar,¹ Bruno Ramoa,^{1,2}
Thomas Lucyshyn ³, Michael Feuchter ³, Gerald Pinter ³, Vito Speranza ⁴,
and Roberto Pantani ⁴

¹Polymer Competence Center Leoben GmbH, Roseggerstrasse 12, Leoben 8700, Austria

²Institute for Polymers and Composites, University of Minho, Campus de Azurém, Guimarães 4800-058, Portugal

³Department of Polymer Engineering and Science, Montanuniversität Leoben, Otto-Gloeckl Strasse 2, Leoben 8700, Austria

⁴Department of Industrial Engineering, University of Salerno, Via Giovanni Paolo II, Fisciano (SA) 84084, Italy

Correspondence should be addressed to Michael Berer; michael.berer@pccl.at

Received 14 January 2022; Revised 23 February 2022; Accepted 24 February 2022; Published 23 March 2022

Academic Editor: Zefan Wang

Copyright © 2022 Theresia Schrank et al. This is an open access article distributed under the Creative Commons Attribution License, which permits unrestricted use, distribution, and reproduction in any medium, provided the original work is properly cited.

It is well known that the processing conditions in polymer processing have a high impact on the resulting material morphology and consequently the component's mechanical behavior. However, especially for semicrystalline polymers, the tools available for predicting the final morphology of injection molding parts still have significant limitations. In order to investigate the potential of injection molding simulation for the prediction of the morphology, POM homopolymer specimens were injection molded. The crystallization kinetics data were measured, and simulations in 3D and 2.5D with and without crystallization analysis were conducted in Autodesk Moldflow. The simulations are found to be good accordance with the experiments. Predicted spherulite size and crystalline orientation factor reveal a good qualitative correlation with optical micrographs. Also, the evolution of these parameters along the flow path is plausible. The simulation is found to be a powerful tool for morphology prediction in polymeric parts. Its applicability, however, is still limited to 2.5D models in Autodesk Moldflow, which, of course, is insufficient for complex, thick-walled 3-dimensional parts.

1. Introduction

The thermoplastic polymer polyoxymethylene (POM) is used in a broad field of structural applications such as bearing rolls and gear wheels and in the automotive industry. It shows excellent (fracture) mechanical and tribological properties along with very good wear resistance and dimensional stability [1–10].

The dominant processing method for POM and polymers in general is injection molding. Short cycle times, high repeatability, and the possibility to partly or even fully automatize the process make it an excellent choice for high volume production. Additionally, a rather high geometrical freedom is given. Parts from very small to very large size and

mass can be produced. The processing parameters during injection molding play a crucial role in the determination of the performance of the future part. There is a strong correlation between process parameters that are set on the machine (input), such as holding pressure, temperature of the heaters, coolant inlet temperature, and cooling time, and resulting processing parameters (output), for example, melt temperature, mold temperature, cooling conditions, and crystallization conditions. These parameters and conditions lead to the morphology, residual stresses, and mechanical properties and therefore the performance of the final part. For standard polymers such as polypropylene, the morphology and mechanical properties of injection molded parts and their correlation have been quite well examined in

the past [11–15]. For POM in specific, also a few studies are available [8, 9, 13, 16–22].

The role of injection molding simulation for filling studies and the prediction of basic processing parameters [23–25] and for the evaluation of optimum processing parameters to, for example, ensure dimensional stability [26–29] has become more and more pronounced over the past years. Furthermore, such simulations allow us to assess the internal stresses that build up during the manufacturing process [23, 30–33]. Especially in complex geometries, the experimental determination of these stresses yields very high experimental effort (if possible at all). The correlation between simulations and experiments was investigated in terms of flow behavior, pressure build up along the flow path, warpage, and residual stresses [30, 34–36]. Although a generally good accordance was stated, it was recommended to include some further aspects in the simulations for more precise results. This includes the geometry of the nozzle and that the effect of pressure on the viscosity of the material must not be neglected [35, 37]. Besides the influence of mold temperature [38–41], it is also known that the application of shear on the melt during the injection molding process strongly affects the crystallization behavior (flow-induced crystallization) and, as a consequence, the morphology of semicrystalline polymers [42–47]. Shear deformation leads to stretching of the molecules and a higher nucleation rate [48] and, subsequently, to smaller spherulitic structures. Above critical values of molecular stretch and mechanical work, the formation of shish-kebab structures is induced [49]. At the present, in the commercial injection molding simulation tool Autodesk Moldflow, crystallization analysis is implemented but not frequently applied due to the need to determine the crystallization model parameters. As a consequence, only a few research studies have been performed on this topic. The determination of the layer morphology of an injection molded part by evaluating the crystalline orientation factor was done by Andreasson et al. [50]. Li et al. [51] conducted a more detailed study on the influence of crystallization on warpage of a PP and a PP/EPDM blend. For PP, also studies combining experimental injection molding and simulation with crystallization analysis are available. Pantani et al. [52] employed microscopy, infrared, and X-ray analysis to compare experimental crystallinity, orientation, and crystal structure measurements to simulations. The effect of packing pressure on the evolution of morphology and orientation was characterized by experiments and simulations in [53]. Liparoti et al. [54] investigated the effect of mold temperature on the morphological and mechanical properties of PP. The injection molding simulation in [52–54] was done using a code developed at the University of Salerno. A study employing Moldflow for the simulation of samples with nonsymmetric mold temperatures is also available [55]. Simulated shear and temperature profiles were compared to morphological and mechanical measurements.

In the present study, tensile specimens were injection molded following a design of experiments (Doe). Injection molding simulations in 3D and 2.5D were carried out for all conditions of the Doe with Autodesk Moldflow Insight 2019

(“Moldflow” in the following discussion) (Autodesk, Inc., California, USA). Simulations and experiments were compared in terms of fill time, peak injection pressure, and in-cavity pressure to assess the quality of the simulations. Additionally, crystallization kinetics modelling was conducted within the 2.5D simulations. The parameters for the crystallization model in Moldflow were experimentally assessed in advance. This resulted in three different simulation approaches: 3D simulations, 2.5D simulations with crystallization kinetics modelling (2.5D C), and 2.5D simulations without crystallization kinetics modelling (2.5D NC). The potential for predicting the morphology of the final part quantitatively was evaluated by analyzing simulated spherulite sizes and the crystalline orientation and by their comparison to experimental data.

2. Experimental

2.1. Materials. The material used in this study was a polyoxymethylene homopolymer with the trade name Delrin 111PF, a member of the Delrin 100 series from DuPont (DuPont, Wilmington, Delaware, USA). It is suitable for injection molding, is highly crystalline, has good toughness and impact behavior, high stiffness, and outstanding creep and fatigue resistance. The 111PF resin is modified in terms of additives; amongst others it contains a heterogeneous nucleation agent, which significantly alters its crystallization behavior. A molar mass of 146,000 g/mol and a polydispersity index of 2.6 were determined and published previously for this material [9].

2.2. Injection Molding Experiments. In this study, tensile specimens according to ISO 527 were injection molded. Processing was conducted on a Battenfeld HM 110/350H 130 V (Wittmann Battenfeld GmbH, Kottlingbrunn, Austria) injection molding machine with a two-cavity mold (Figure 1). Before feeding the pellets into the barrel, they were dried for 2 h at 80°C in a hot air dryer. The processing parameters were varied following a full factorial 2³ Design of Experiments (Doe), where high and low levels of packing pressure, temperature profile along the barrel, and mold temperature were set. This resulted in a total of 8 processing conditions (C1–C8). An in-cavity pressure sensor at the end of the flow path was used for pressure-controlled switch-over. In Table 1, important processing parameters and the 2³-factorial Doe parameters are given. An illustration of the temperature profile is depicted in Figure 2. The temperature of the mold was measured with a contact thermometer at the opened mold.

2.3. Polarized Optical Light Microscopy. To compare the crystalline features of the experimentally injection molded specimens to the results of the injection molding simulation, optical light microscopy was carried out. Films with a thickness of 10 μm were cut from the cross section of the tensile specimens with a microtome (Reichert Jung, Heidelberg, Germany). The films were analyzed with polarized light in transmission mode on an Olympus SZX12 stereo



FIGURE 1: Injection molded part from the two-cavity mold including the runner system and the two tensile specimens.

TABLE 1: Injection molding conditions following a 2³-factorial design of experiments with a flow rate of 15 cm³/s and a holding time of 30 s for all conditions.

Processing condition	Switch-over pressure (MPa)		3.5 (C1–C4)	Coolant inlet temperature (°C)
	Packing pressure (MPa)		2.5 (C5–C8)	
C 1	60		–1	50
C 2	110		–1	50
C 3	60		+1	50
C 4	110		+1	50
C 5	60		–1	110
C 6	110		–1	110
C 7	60		+1	110
C 8	110		+1	110

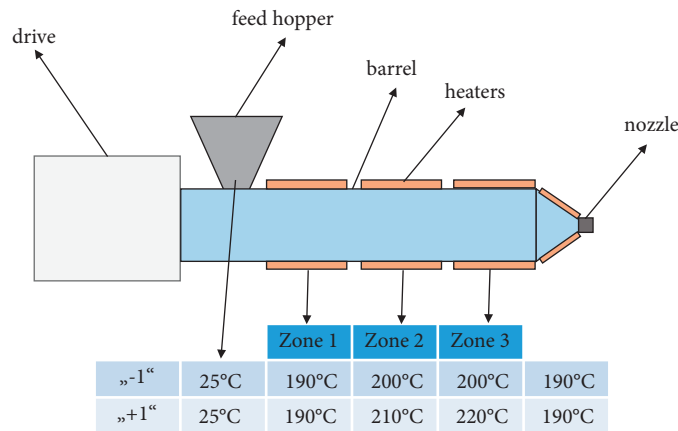


FIGURE 2: Temperature settings for the profile “–1” and “+1” along the barrel of the injection molding machine.

microscope (Olympus Corporation, Tokyo, Japan). The positions, where the films were cut from the tensile specimens, were chosen according to the evaluation positions of the simulations.

3. Injection Molding Simulation

3.1. *Simulation Model.* Injection molding simulation was carried out with the software Autodesk Moldflow Insight 2019 (Autodesk, Inc., San Rafael, California, USA). A 3D model of the tensile specimens was built and then meshed with tetrahedral elements with a global edge length of 2 mm and at least 10 elements over the thickness (Figure 3(a)). The quality of the 3D mesh was assessed by the aspect ratio and

the maximum dihedral angle of the elements. 7 elements were found to exceed the maximum aspect ratio of 50 suggested in Moldflow [56]. Nevertheless, these elements were found at the end of the flow path and hence not considered critical. The maximum dihedral angle was found to be 176.9°, which is also below the critical value of 178°. Since crystallization analysis in Moldflow is only available for 2.5D simulation (dual-domain and midplane mesh), the 3D model was transformed into a dual-domain model and meshed with triangles with a global edge length of 0.66 mm to obtain also a 2.5D simulation model (Figure 3(b)). The aspect ratios of all elements were found to be below the critical value, the mesh match ratio was above 90%, and no non-oriented elements were found. This made the mesh

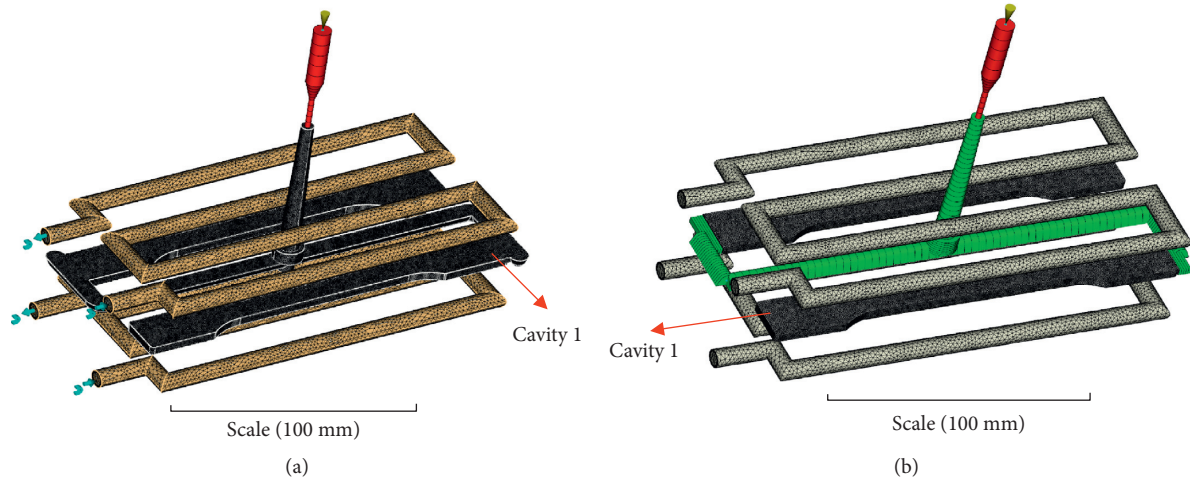


FIGURE 3: Moldflow models of the cavity, runner, sprue, and nozzle for the 3D (a) and 2.5D (b) simulations.

suitable for 2.5D simulation. The models consisted of the two tensile specimen cavities, the runner, the sprue, and the nozzle. The runner and the sprue were modelled as cold runner beam elements for the dual-domain model. The nozzle, represented by a hot runner, was also included in both models, as this is expected to lead to more accurate simulation results [35, 44]. Additionally, the mold block made of tool steel “P-20” and the cooling system were included in the model. During processing, the mold temperature was altered according to the Doe by changing the temperature of the cooling fluid. Consequently, in the simulation, this change was implemented identically using the “coolant inlet temperature” parameter. For the experimental evaluation, only tensile specimens from one cavity (cavity 1 as marked in Figure 3) were used. Simulation evaluations were also carried out on this cavity.

Simulations in 3D, 2.5D with crystallization kinetics modelling (2.5D C), and 2.5D without crystallization kinetics modelling (2.5D NC) were conducted. The input settings for the processing parameters were taken from the described experimental injection molding process and Doe (section 2). For the simulations, the Doe parameter “temperature profile” had to be converted into two single melt temperature values, i.e., 200°C and 215°C, respectively, which are the average values of the barrel zones 3 and 4 in Figure 2. These two values were considered as adequately representative for the melt temperatures, although not directly measured during the process. They were implemented in the simulations as the initial temperature of the melt when it entered the nozzle. The temperature of the nozzle itself was set to 190°C in the simulations.

3.2. Material Model. For the POM homopolymer resin used in our study (Delrin 111 PF), a Moldflow material database on the basis of experimental data was developed. The corresponding material characterization was performed by the Department of Industrial Engineering at the University of Salerno in Italy (subsequently termed as “DIIn Salerno”). The material characterization included the quantitative

determination of rheological parameters as well as a quantitative study of the crystallization kinetics. A brief overview of the methods used is described in the following.

Firstly, a rheological characterization of the POM resin was carried out by using a rotational and capillary rheometer. In order to mathematically describe the shear thinning behavior of the polymer melt over a wide range of shear rates, a Cross-WLF model (1) and (2) was adopted, in which, the melt viscosity η is described as a function of the zero shear viscosity η_0 , the shear rate $\dot{\gamma}$, the critical stress level at the beginning of shear thinning τ^* , and the power law index n at high shear rates. The zero shear viscosity η_0 is a function of the temperature T , the pressure P , and the fitting parameters D_1 , D_2 , D_3 , A_1 , and A_2 .

$$\eta(T, P, \dot{\gamma}) = \frac{\eta_0(T, P)}{1 + (\eta_0(T, P) \cdot \dot{\gamma} / \tau^*)^{1-n}}, \quad (1)$$

$$\eta_0(T, P) = D_1 \times \exp\left(-A_1(T - D_2 - D_3P) / A_2 + T - D_2 - D_3P\right). \quad (2)$$

The results of the rheological measurements are shown in Figure 4. The parameters adopted to describe the measurements by the Cross-WLF model are reported in Table 2.

Secondly, the crystallization behavior of the Delrin 111PF was investigated in quiescent and under flow conditions. The POM crystallization kinetics was described adopting the Kolmogorov–Avrami–Evans (KAE) model. In particular, the model assumed that the growth rate and the homogeneous nucleation rate depend only on temperature and follow the Hoffman–Lauritzen theory. Moreover, the presence of a heterogeneous nucleation, also dependent upon temperature, was considered in the model. The application of flow conditions was found to considerably increase the growth rate but did not significantly affect the nucleation rate. A more detailed description of the crystallization model, the measurement methods of these data, and the assumptions and simplifications will be published in the future.

More relevant for the present study was the transfer of the crystallization kinetics data into the parameters of the

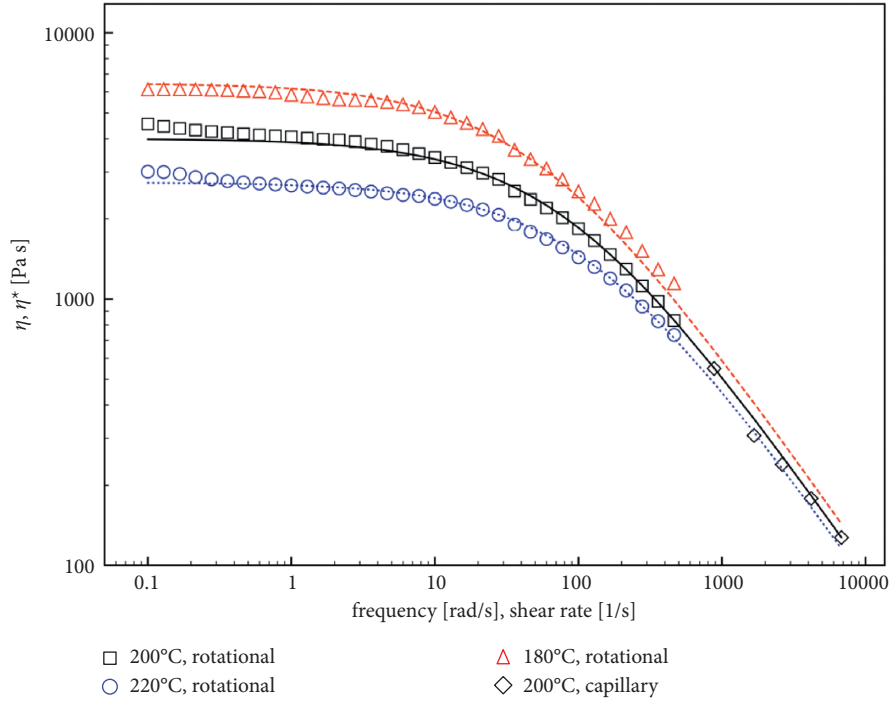


FIGURE 4: Results of the rheological measurements (rotational and capillary rheometer), which were used to fit Equations (1) and (2).

TABLE 2: Results for the fitting parameters of the Cross-WLF model (using the rheological data from Figure 4).

Parameter	Value
n [-]	0.227
τ^* (Pa)	330910
D_1 [Pa*s]	3990
D_2 (K)	473
D_3 (K/Pa)	7.63E-08
A_1 [-]	3.37
A_2 (K)	160

crystallization model adopted by Moldflow [56]. In this Moldflow model, the presence and formation of nuclei under both quiescent conditions and shear flow are taken into account. The growth rate is determined following the Hoffman–Lauritzen theory [57, 58]. The equation for the temperature-dependent crystal growth rate is given in (3), where the pre-exponential factor G_0 and the kinetic K_g are material-specific constants that are determined under quiescent conditions and T_m^0 is the resin-specific, pressure-dependent equilibrium melting temperature, which is a function of the equilibrium melting temperature T_{eq} , the pressure P , and the grade-specific constant b_6 . T_∞ is the temperature 30 K below the glass transition temperature T_g , U^* is the activation energy of motion, and R_g is the gas constant.

$$G(T) = G_0 \exp\left[-\frac{U^*}{R_g(T - T_\infty)}\right] \exp\left[-\frac{fK_g}{T(T_m^0 - T)}\right], \quad (3)$$

$$f = \frac{(T + T_m^0)}{2T}. \quad (4)$$

Using Equation (3) to fit the growth rate obtained from the crystallization kinetics characterization, it was possible to derive the aforementioned material- and resin-specific constants.

The nucleus generation in Moldflow is calculated as the sum of nuclei activated under quiescent conditions N_0 and nuclei induced by shear flow N_f (Equation (5)).

$$N = N_0 + N_f. \quad (5)$$

The number of activated nuclei in the quiescent condition is assumed to be a unique function of the supercooling temperature $\Delta T = (T_m^0 - T)$ and is described by

$$\ln(N_0) = a_N(T_m^0 - T) + b_N, \quad (6)$$

where a_N and b_N are the material- and resin-specific constants.

The number of flow-induced nuclei as implemented in Moldflow is given by Equation (6) [59]. Here, N_f is the nucleation rate induced by the flow, λ_N is the relaxation time, C_0 is a constant, and k_B is the Boltzmann constant. ΔF_q and ΔF_f are parameters describing the free energy, q is a fitting

index, and $\varphi(T)$ is a function of the temperature T and the equilibrium melting temperature T_m^0 . ϑ is a function of the

temperature T , T_m^0 , and the melting enthalpy of a purely crystalline material ΔH_0 .

$$\dot{N}_f + \frac{1}{\lambda_N} N_f = C_0 k_B T \exp\left[-\frac{U^*}{R_g(T-T_\infty)}\right] \left\{ (\Delta F_q + \Delta F_f)^q \exp\left[-\frac{\phi(T)K_g}{2T^2[(1+\vartheta(\Delta F_f)^q)T_m^0 - T]}\right] - \Delta F_q \exp\left(-\frac{\phi(T)K_g}{2T^2 \Delta T}\right) \right\}. \quad (7)$$

In order to describe the observed POM crystallization behavior, a_N and b_N were determined by assuming that the number of activated nuclei in the quiescent condition is identical to the number of heterogeneous predetermined nuclei. Furthermore, the nucleation rate due to the flow was assumed equal to the homogeneous nucleation rate. To this aim, in (6) $q=0$ and $\lambda_N \rightarrow \infty$ were considered. With these assumptions, the constant C_0 remained the only free parameter in (6), which had to be determined to describe the observed POM crystallization kinetics. The final parameters obtained for the crystallization model of the material in Moldflow are summarized in Table 3.

The effect of crystallinity on the viscosity of the material was also considered in the Moldflow crystallization kinetics modelling according to Equation (8) [59, 60]. Here, η is the viscosity of the system, η_a is the viscosity of the amorphous phase, α is the relative crystallinity, and A , β , and β_1 are the parameters describing the effect of the crystallinity on the viscosity of the system. Measuring the effect of crystallinity on the viscosity yields very high experimental effort and requires equipment, which were not accessible within this project. Therefore, for our simulation models, the corresponding parameters had to be deduced from previous studies at the DIIn Salerno conducted on other polymers. This resulted in the values $A=1.66$, $\beta=14.615$, and $\beta_1=1$, which were subsequently used in the simulations.

$$\frac{\eta}{\eta_a} = 1 + \frac{(\alpha/A)^{\beta_1}}{(1-\alpha/A)^\beta}. \quad (8)$$

4. Results and Discussion

4.1. Filling. The fill times obtained experimentally from the injection molding process (experimental) and the simulated fill times for the 3D simulations and the 2.5D simulation with and without crystallization kinetics modelling are displayed in Figure 5. The deviations between the different conditions are very small and in the order of tenths of seconds for both experiments and simulations. Therefore, for the studied geometry, the chosen processing parameters do not have a significant influence on the fill time, when filled with a constant flow rate.

It is obvious from Figure 5 that the 3D simulations calculate a faster filling than the 2.5D simulations. This is due to the different modelling of the cavity. In 2.5D, the runner and the sprue had to be made of beam elements since the half-elliptical geometry could not satisfyingly be modelled with a dual-domain mesh. Therefore, the cavity volume slightly changed from 31.7 cm^3 (3D) to 36.9 cm^3 (2.5D),

leading to a fill time difference of about 0.4 s, when filled with a flow rate of $15 \text{ cm}^3/\text{s}$. When comparing the experimental fill times with the simulated ones, it is obvious that the simulated fill times are smaller (except for the 2.5D models, which have a slightly bigger volume). This is a more generally observed effect: fill times are underestimated by injection molding simulation since the machine's inertia, internal delays (e.g., electrical delays), or decreased performance due to wear are not considered.

4.2. Injection Pressure. The peak injection pressures obtained from the experiments and simulations are compared in Figure 6. Since the cavity is filled with the same flow rate for all conditions, the injection pressure during processing is expected to vary as a consequence of the different mold and melt temperatures. An increase of melt temperature results in lower pressure values due to the lower viscosity of the material at higher temperatures. Similarly, a higher mold temperature also decreases the peak injection pressure. The simulations are in good agreement with the experimental values and capture their trend and the quantitative values well (highest deviations are far below 10%). The 3D simulations predict pressures of about 10 MPa higher than measured in the process. It is expected that this slightly increased pressure is a consequence of the smaller filling times obtained in the 3D simulations as discussed above. The 2.5D C simulations suggest slightly higher injection pressures than the 2.5D NC, which indicates an increased viscosity of the melt, when crystallization is considered.

4.3. In-Cavity Pressure. For better orientation in the present and the following sections, a schematic illustration of the cavity and the positions most relevant for the discussion are shown in Figure 7. The red dot marks the position of the in-cavity pressure sensor (which was also the switch-over position), and the blue dot marks the position, where the simulations were evaluated for their thickness-dependent crystalline parameters.

During the processing, the pressure in the cavity was measured at a position 20 mm away from the end of the flow path. The obtained pressure curves from the experiments are displayed in Figure 8. The switch-over pressures for C1–C4 and C5–C8 (p_{switch}) are also included. It is shown that higher mold and melt temperatures prolong the efficiency of the packing pressure, with the effect being less pronounced for the melt temperature. Moreover, by increasing the mold and/or melt temperature, material solidification is efficiently counteracted. Thus, during packing, the pressure drop between the injection point and the position of the in-cavity

TABLE 3: Results of the obtained parameters for the crystallization kinetics model in Moldflow.

Parameter	Value
a_N [$1/m^3K$]	0.75
b_N [$1/m^3$]	4.3284
T_{ceq} (K)	462.5
G_0 (m/s)	7.05
K_g (K^2)	225270
T_g (K)	200
λ_N (s)	$9E + 11$
C_0 [$1/J^2s$]	$1E - 29$

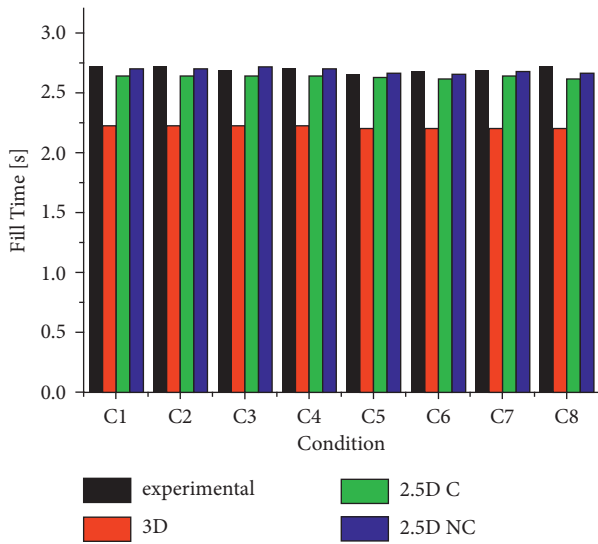


FIGURE 5: Comparison of the fill times obtained from the process (experimental) and the simulations in 3D and 2.5D with and without crystallization kinetics modelling (3D, 2.5D C, and 2.5D NC).

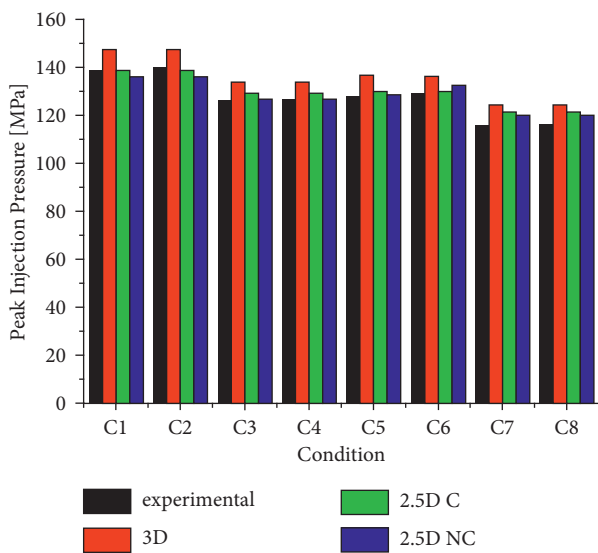


FIGURE 6: Comparison of the peak injection pressures obtained from the process (experimental) and the simulations in 3D and 2.5D with and without crystallization kinetics modelling (3D, 2.5D C, and 2.5D NC).

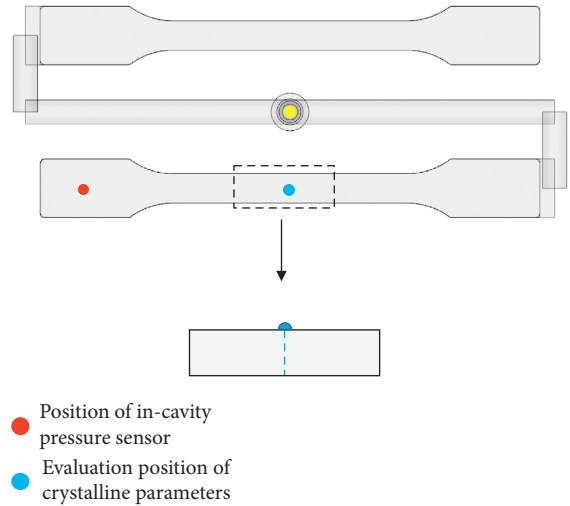


FIGURE 7: Position of in-cavity pressure sensor and evaluation position for the thickness-dependent crystalline parameters.

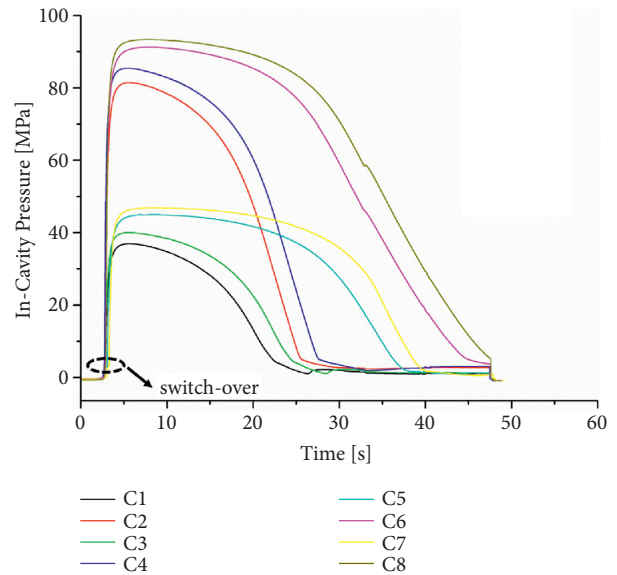


FIGURE 8: In-cavity pressures measured through the pressure sensor at the switch-over position during the processing.

pressure sensor reduces due to the decrease in viscosity. Consequently, the measured in-cavity pressure reaches higher values.

In the following, the number of presented experiments is reduced to four conditions to facilitate the interpretation. When comparing the experimental and simulated in-cavity pressure curves of condition 1 (low mold temperature (T_{mold}), low packing pressure (p_{pack}), low melt temperature (T_{melt}), Figure 9(a)), condition 2 (low T_{mold} , high p_{pack} , low T_{melt} , Figure 9(b)), condition 3 (low T_{mold} , high p_{pack} , high T_{melt} , Figure 9(c)), and condition 5 (high T_{mold} , low p_{pack} , low T_{melt} , Figure 9(d)), it is shown that the 3D and 2.5D C simulations calculate higher pressure levels at the position of the sensor. This is attributed to both, drawbacks in the experiments and the simulations. During the filling of the cavity, the polymer in contact

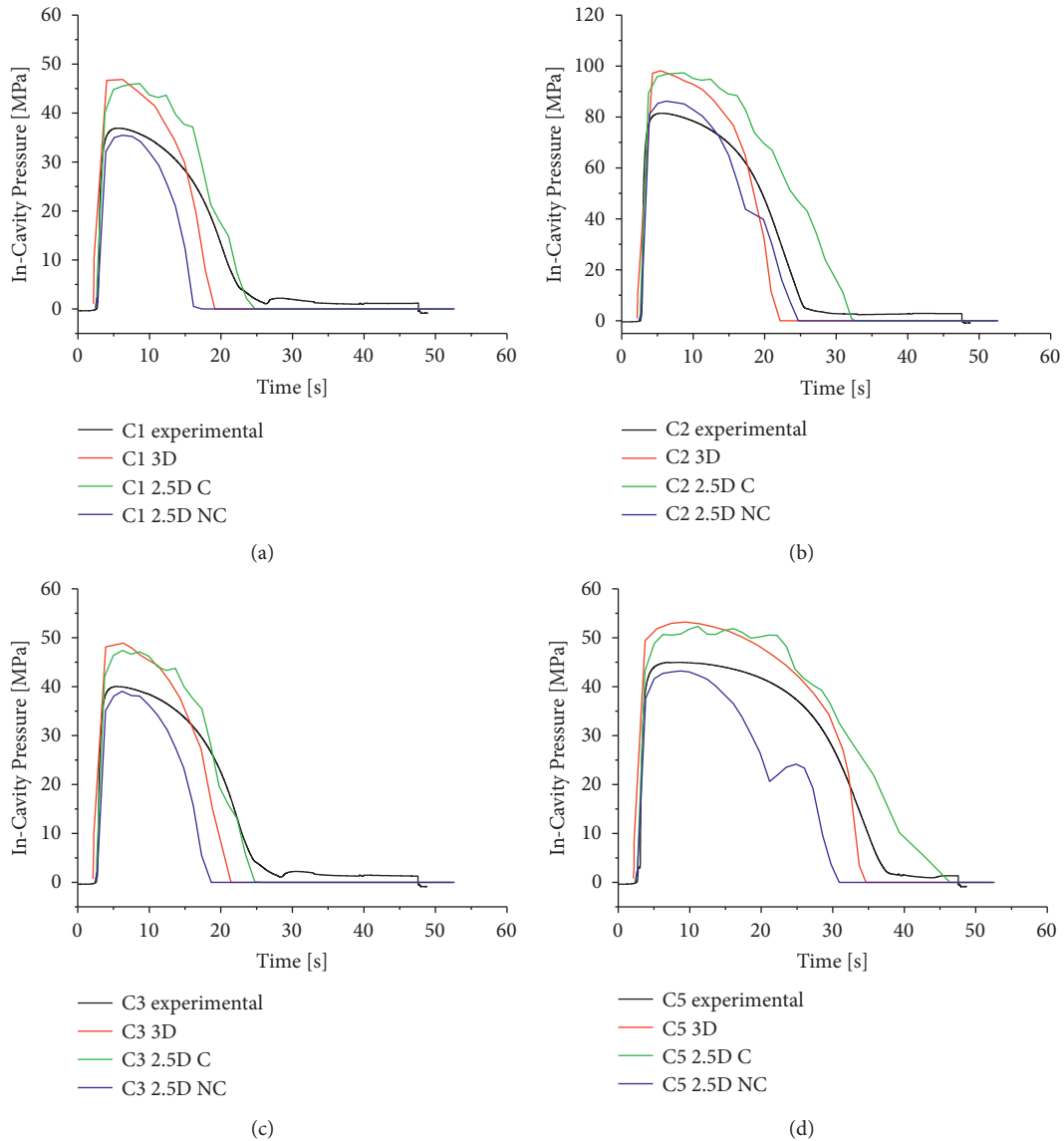


FIGURE 9: Comparison of experimental and simulated in-cavity pressure curves at the switch-over position for the conditions C1 (a), C2 (b), C3 (c), and C5 (d).

with the mold wall freezes very fast. This results in a solid polymer layer, which can shield the pressure sensor from experiencing the full in-cavity pressure and in this way causes smaller pressure values in the measurement. In the simulations on the other hand, the elasticity of the mold was not taken into account. This leads to higher calculated pressures since the elastic expansion of the mold during the process is not considered. It is also worth to mention that the effect of pressure on the viscosity was not measured for the specific material used in this study because of the high experimental effort. However, a small parameter study on the influence of a pressure-dependent viscosity on the simulation results showed a rather small dependence of the simulated pressure curves. Hence, the authors are convinced that this effect can be neglected for the present study. When crystallization is not considered, the 2.5D NC simulations result in lower pressure levels and a

shorter pressure activity duration in the cavity compared with the 2.5D C results. The longer pressure action in the 2.5D C simulations is an indicator for a slower cooling due to the exothermic crystallization process. As a consequence of all these discussion points, the in-cavity pressure evolution at the pressure sensor position is considered to be captured well by the 2.5D C simulations. An even better prediction of the in-cavity pressure values will only be achievable through a drastically higher experimental effort, in particular, through a precise measurement of the pressure and crystallinity influences on the material viscosity. In the 2.5D NC simulations of condition 5 (Figure 9(d)), an increase in the pressure is observed after approximately 20 s. The reason for this effect is not fully understood. It is assumed to be an effect of the combination of the dual domain and the beam elements in the model.

4.4. Final Average Crystal Size. The final average crystal size, which is calculated for the 2.5D simulations with crystallization kinetics modelling, describes the final average size of the spherulites forming during the process (the crystallization kinetics model implemented in Moldflow describes the kinetics of spherulite growth, not to be confused with crystal lamellae growth). Hence, the term “crystal size” is used in the following discussion as a synonym for the spherulite size. Figure 10 displays the simulated spherulite size distribution over the normalized thickness in the middle of the tensile specimen (the blue dot in Figure 7 marks the analysis position). It is shown that the mold temperature is the most significant influence on the spherulite size. At the lower mold temperature setting, a higher packing pressure gives rise to slightly smaller spherulites in the midplane (conditions C2 and C4). At the higher mold temperature setting, this effect can be neglected. The melt temperature variation had only a negligible effect on the spherulite size distribution. The decrease of the spherulite size predicted in the middle of all specimens is attributed to different crystallization conditions in this region. Shear decreases towards the midplane, and therefore the effect of shear flow on the spherulitic growth diminishes. This effect was also reported for PP [61].

The simulations predict rather small spherulite sizes. This reflects well the situation in the injection molded samples: the spherulites are very small and coalesce, and hence, their size could not be quantified, neither by optical light microscopy nor by SEM analysis of chemically etched samples. However, it is possible to distinguish different layers over the cross section of the samples in both, the simulated spherulite sizes and light microscopically generated micrographs. As shown in Figure 10, the crystal size is mainly dependent on the mold temperature and the packing pressure. Therefore, only data for condition 1, condition 2, and condition 5 will be discussed in the following. Overlays of these three are shown in Figure 11(a) for condition C1 (low T_{mold} , low p_{pack}), Figure 11(b) for condition C2 (low T_{mold} , high p_{pack}), and Figure 11(c) for condition C5 (high T_{mold} , low p_{pack}). The micrographs were cut at the evaluation position of the crystalline parameters according to Figure 7. Near the mold wall, a skin layer with apparently lower crystallinity and smaller spherulite sizes was formed due to the rapid cooling in this area. For the higher mold temperature setting, this layer is less pronounced. The simulation reflects this skin layer very well for the lower mold temperature setting, predicting an area with rather uniform and very small spherulites. For the higher temperature setting, the “over-the-thickness resolution” in the simulation is too low to get more than one data point in this layer. An interesting aspect of the skin layer is that it is transparent to optical light, which indicates that the spherulites in this region are smaller than the wavelength of visible light. The simulations for all three conditions, C1, C2, and C5, predict spherulite sizes below 250 nm in the corresponding region, which is clearly below the smallest wavelength in the visible spectrum. Thus, the transparency of the skin layer is correctly predicted by the 2.5 D simulation with crystallization kinetics modelling. Beneath this low crystallinity skin layer,

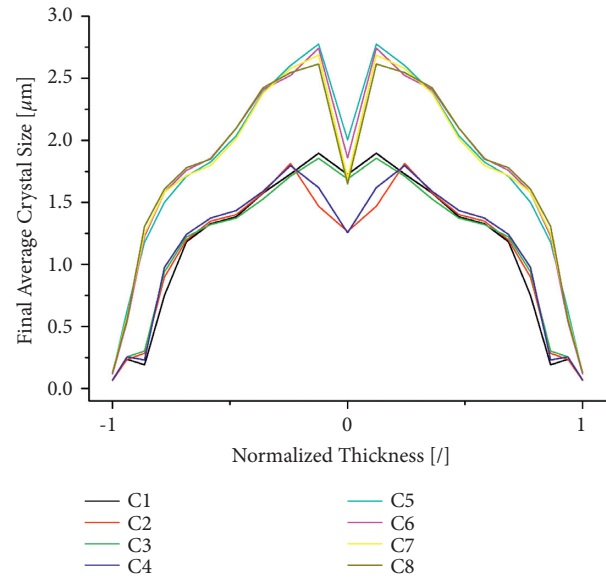


FIGURE 10: Simulated final average crystal sizes in the middle of the tensile specimen.

an increase of the spherulite size is observed in the simulations. The experimental micrographs also suggest an increasingly dense spherulitic structure towards the specimen center. The optical change in the morphology as it is also predicted by the simulations. Overall, the micrographs for all conditions at the lower mold temperature setting (C1–C4) were rather similar. No apparent influence of packing pressure or melt temperature could be determined from these micrographs, although indicated in the simulations. The same was also observed for the higher mold temperature setting (C5–C8). Hence, the mold temperature was the only significant influence, which was identified.

From the optical micrographs in the middle of the tensile specimens, the thickness of the skin layer was measured and divided by the specimen’s thickness to obtain the skin ratio (Figure 12). It is obvious that the mold temperature is the dominating processing parameter here. This is in good accordance with the findings from the simulations (Figure 10), where also the influence of the mold temperature was found to be the most significant.

The distribution of the final average crystal size over the specimen’s thickness along the flow path is depicted in Figures 13(a) and 13(b) for the conditions C1 and C5, respectively. The simulations suggest a rather flow path-independent spherulite size distribution with small differences only in the area near the mold wall. These differences are more pronounced for the lower mold temperature setting (condition C1). Here, the thickness of the skin layer with rather small spherulites decreases significantly from the “gate” to the “middle,” whereas no further difference is observed between “middle” and “end.” The explanation for this skin layer difference along the flow path is that the closer to the gate, the earlier the melt front reaches the corresponding area during filling and consequently the more melt passes it until the cavity is full. In this way, more near surface

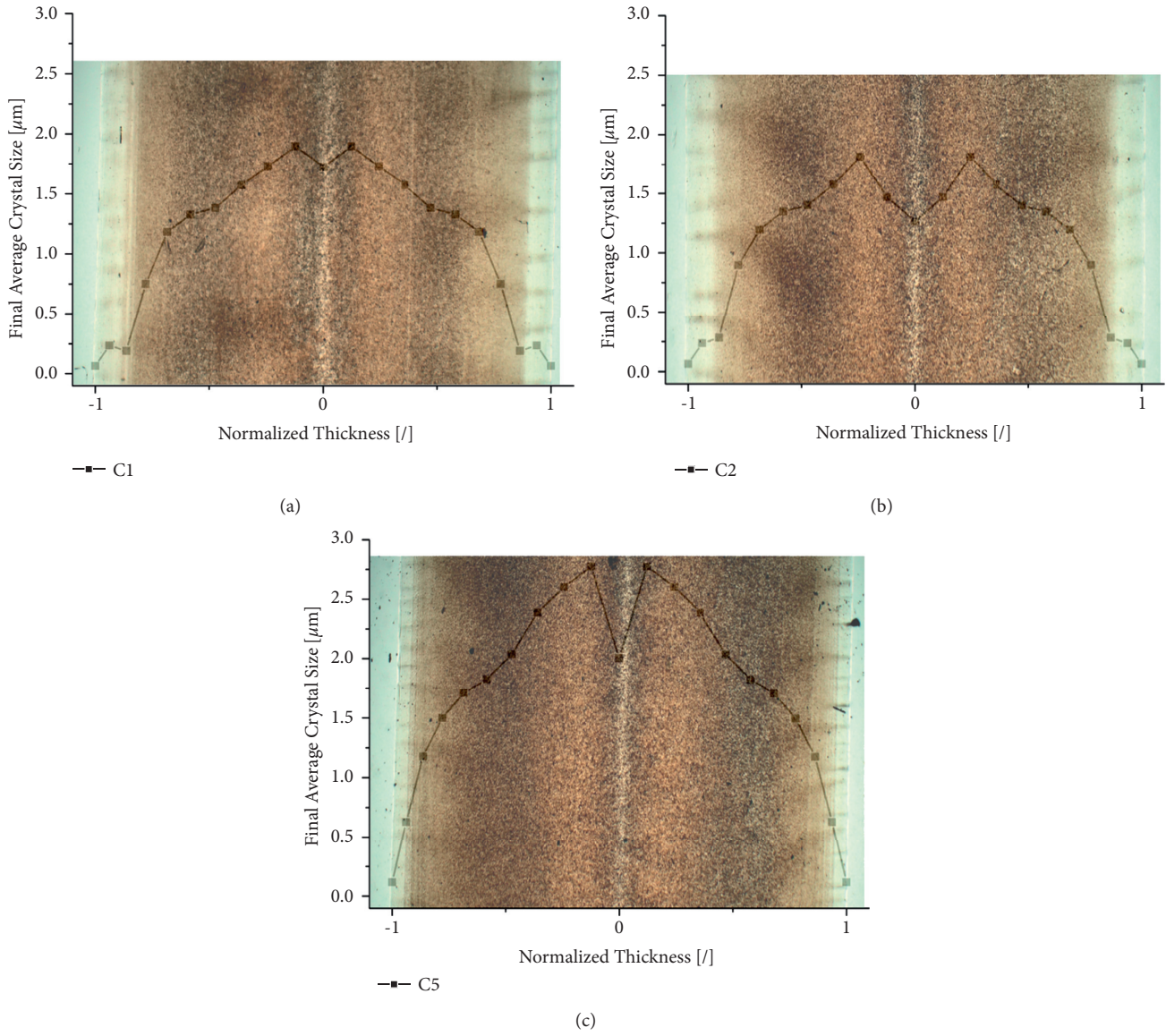


FIGURE 11: Final average crystal size in the middle of the tensile specimen for conditions (a) C1, (b) C2, and (c) C5.

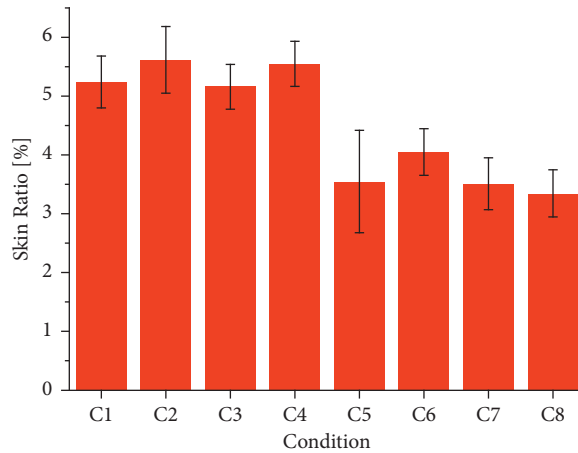


FIGURE 12: Skin ratios for all processing conditions obtained from the experimental micrographs (arithmetic average of 8 measurements, error bars represent standard deviation).

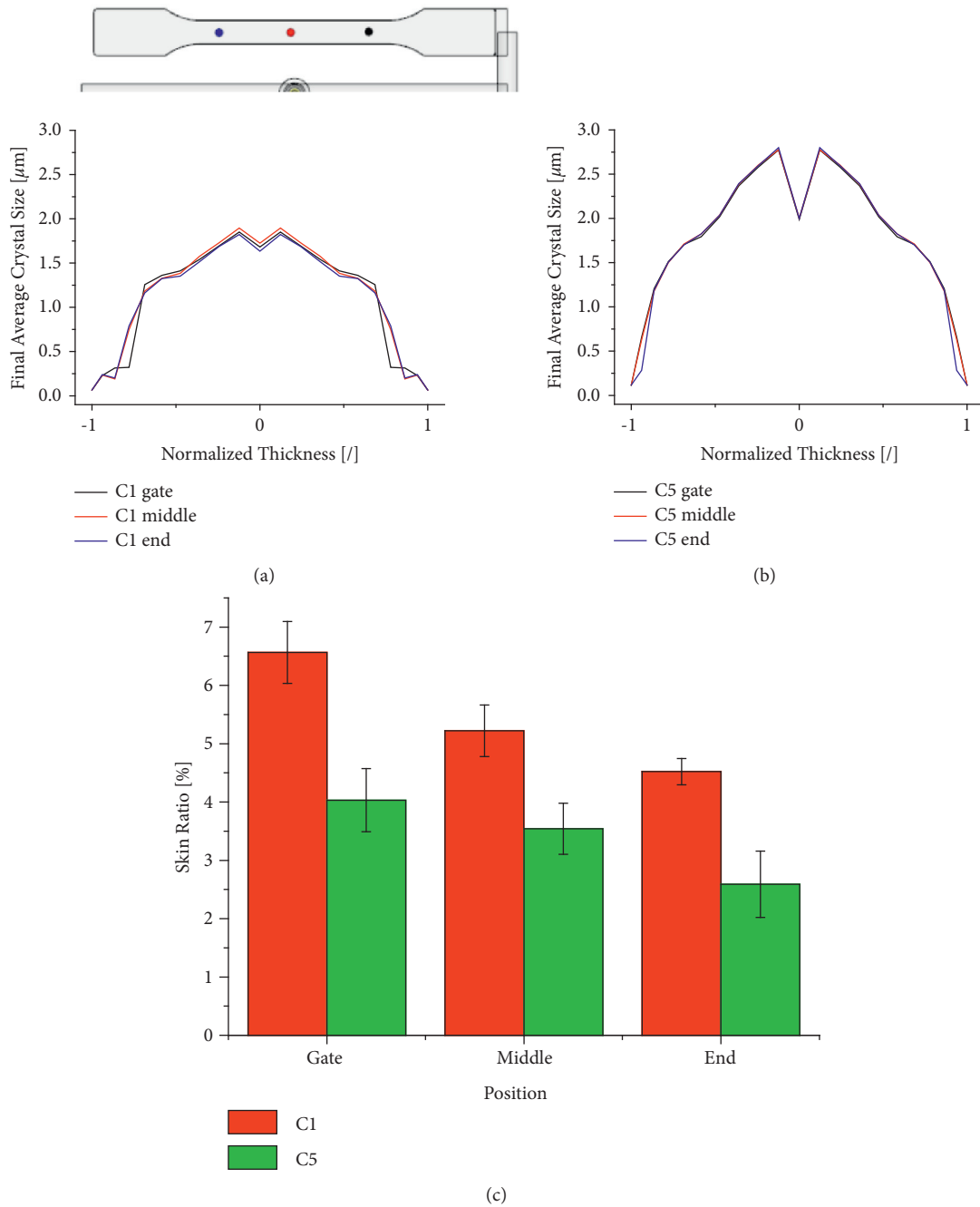


FIGURE 13: Final average crystal size along the flow path for the two conditions C1 (a) and C5 (b) and (c) skin ratio for the conditions C1 and C5 at the three selected analysis positions along the flow path (arithmetic average of 8 measurements, error bars represent standard deviation).

material of the melt shear flow is frozen on the mold wall, which finally leads to thicker skin layers in these areas.

Additionally, experimental micrographs from the positions shown in Figure 13 (gate, middle, and end) are made. Figure 13(c) depicts the skin ratio at these three positions for conditions C1 and C5. The skin ratio and therefore the skin thickness decrease along the flow path. This supports the findings from the simulations shown in Figures 13(a) and 13(b). For C1, the experimental skin ratio decreases from

6.6% at “gate” to 5.2% at “middle” to 4.5% at “end,” whilst the simulations do not show a change from “middle” to “end.” C5, on the other hand, shows a decrease from 4% at “gate” to 3.5% at “middle” to 2.6% at “end” in the experiment and no change from “gate” to “middle” in the simulations. Regarding these small deviations between experiment and simulation, it is assumed that the resolution of the simulation is simply not high enough to represent these small changes in the skin layer precisely. Nevertheless, the results

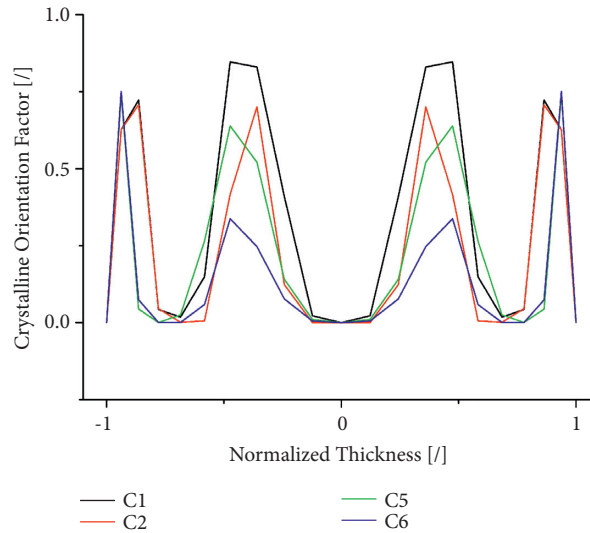


FIGURE 14: Simulated crystalline orientation factor in the middle of the tensile specimen for the conditions C1, C2, C5, and C6.

are in good accordance and the simulations predict the thickness of the skin layer acceptably well.

4.5. Crystalline Orientation Factor. The crystalline orientation factor (COF) in Moldflow is an indicator for the orientation of the crystals. It can reach values between -0.5 and 1 , where -0.5 refers to perfect orientation perpendicular to the flow direction, 0 represents random/no orientation, and 1 perfect orientation in flow direction. In Figure 14, the COF distributions for the conditions C1, C2, C5, and C6 are shown. The diagram was reduced to these four conditions since the melt temperature range used in our study was found to have only little influence on the crystalline orientation in this case. In the area near the mold wall, the crystals show a preferred orientation in the flow direction. The thickness of this near surface layer is strongly dependent on the mold temperature. A lower mold temperature setting results in a thicker oriented layer at the specimen's surface. The reason for this is the higher difference between mold and melt temperature and therefore the higher cooling rate in this area. Orientations are frozen almost immediately and are not able to relax afterwards. A higher melt temperature (not shown in Figure 14) leads to a slightly lower orientation near the mold wall for the low-mold-temperature setting. The packing pressure has no influence on this region since it develops during filling and has already solidified when the packing phase starts. This oriented skin region is followed by a randomly oriented layer and subsequently an inner layer again oriented in flow direction. This second oriented layer is strongly dependent on both, the mold temperature and the packing pressure. Higher mold temperatures and higher packing pressures lead to a decreasing orientation in flow direction in this area. For higher mold temperatures, the polymer stays in the molten state for a longer time, which gives the orientations more time to relax. Surprisingly, a higher packing pressure does not introduce additional orientation in the simulation results. In contrary, it decreases

the thickness and orientation level of the inner oriented layer. It is speculated that this is an effect of additional hot melt forced into the cavity during packing. In this way, the material is kept longer above the solidification temperature, and hence, the orientations have more time to relax. From the experimental point of view, the inner oriented layer in the simulations is attributed to the so-called shear layer, which is a typical morphological characteristic of injection molded samples [9, 62]. Additionally to the simulated COF results, experimental orientation measurements by wide-angle X-ray diffraction (WAXD) were also conducted. There, Hermann's orientation factor (HOF) was evaluated. However, the HOF refers to the orientation of the (100) crystal planes, whilst the crystallization results in Moldflow are calculated with kinetics data on a spherulitic level. Therefore, the comparability of these two parameters is questionable and the presentation of experimental orientation results is foregone in this study.

In analogy to the final average crystal size, the simulated crystalline orientation factors were also evaluated at the three positions "gate," "middle," and "end" along the flow path (Figure 15). For both mold temperature settings, a decrease of the crystalline orientation can be observed along the flow path. Thickness and orientation in flow direction of both oriented layers get smaller from the "gate" to the "end". On the one hand, this is attributed to the different flow and shear conditions during the filling stage. During filling, the maximum shear rate is usually near the mold wall. At the position "gate," which is filled first, the material that is in contact with the mold wall solidifies rather fast. The cross section of the cavity is reduced, and the position of the maximum shear rate is shifted inwards. This results in the increased thickness of the outer oriented layer. The effect is more pronounced for the lower mold temperature setting since the solidification of the material is much faster here. On the other hand, the steadily reduced cross section towards the gate (through frozen material) results in both increasing shear rates and higher orientations.

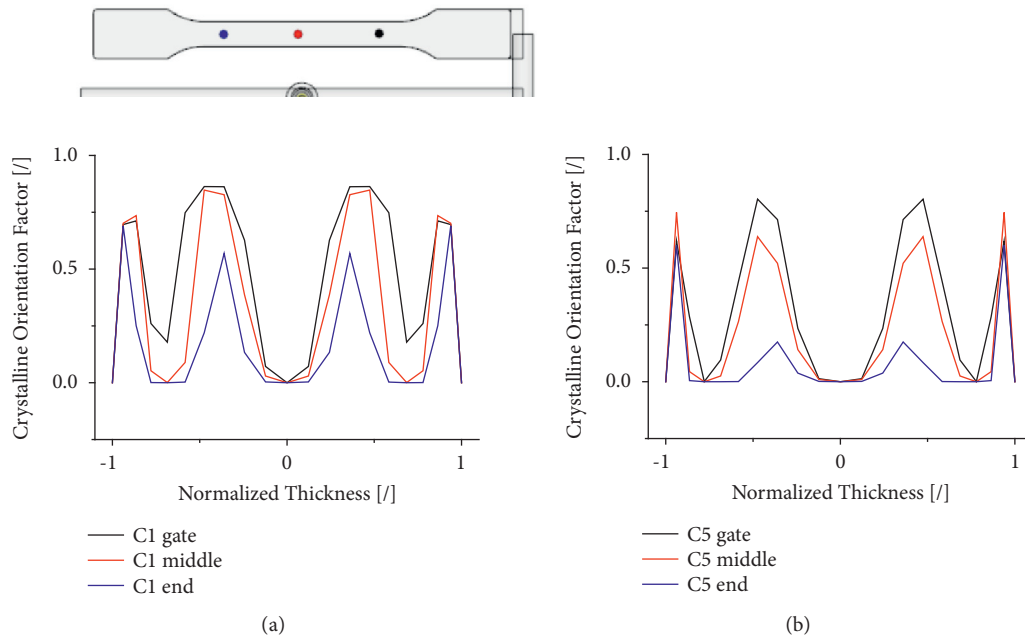


FIGURE 15: Crystalline orientation factors along the flow path for the conditions C1 (a) and C5 (b).

Consequently, the shear rate decreases along the flow path in the filling as well as in the packing phase, resulting in a decreased orientation in flow direction along the flow path. For the inner oriented layer, a larger orientation decrease is predicted for the higher mold temperature setting due to a smaller cross-section reduction and a higher melt solidification (and thus relaxation) time in this case.

5. Conclusion

In general, a good accordance between injection molding experiments and simulations in terms of fill time, maximum injection pressure, in-cavity pressure, and final average crystal size was achieved. A further improvement is expected by a more detailed monitoring of the injection molding process, for example, melt temperature measurement. For the simulation models, the pressure dependence of the viscosity and the influence of crystallization on the viscosity had to be estimated due to general experimental limitations in these fields. The crystallization results appear promising in terms of crystal size and crystalline orientation, although the latter could not be experimentally proved.

Unfortunately, the determination of the whole crystallization kinetics data set yields rather high experimental effort. It is shown in this study that the injection molding simulation including the crystallization kinetics modelling produces useful results in terms of spherulite size and crystalline orientation. Nevertheless, for basic injection molding simulation applications, for example, filling studies, the effort to determine this parameter set is far too high. Moreover, the crystallization analysis tool in Moldflow is currently only available for 2.5D simulation models. This further limits its application to rather simple geometries and introduces errors for more complex parts. According to the

Moldflow support, an integration of this tool for 3D simulations is not planned currently since the commercial demand seems to be rather low at the moment.

In the future, the tensile specimens produced in this study will be analyzed in detail in terms of morphology and mechanical behavior and the results will be presented in a follow-up publication. Additionally, a subsequent study will be carried out on smaller specimens, very thin platelets, which will be injection molded under harsher processing conditions.

Data Availability

The data used to support the findings of this study are currently under embargo, while the research findings are commercialized. Requests for data, 12 months after publication of this article, will be considered by the corresponding author.

Conflicts of Interest

The authors declare that they have no conflicts of interest.

Acknowledgments

The research work of this paper was performed at the Polymer Competence Center Leoben GmbH (PCCL, Austria) within the framework of the COMET and BRIDGE1-programmes of the Federal Ministry for Climate Action, Environment, Energy, Mobility, Innovation and Technology and the Federal Ministry for Digital and Economic Affairs with contributions by the Montanuniversitaet Leoben (Institute of Materials Science and Testing of Polymers) and the University of Salerno (Department of Industrial Engineering). The PCCL was funded by the Austrian Government

and the State Governments of Styria, Lower Austria, and Upper Austria.

References

- [1] B. Heym and W. Beitz, "Zur Belastbarkeit von Stirnzahnrädern aus dem Hochtemperatur-Thermoplast PEEK," *Konstruktion*, vol. 47, pp. 351–357, 1995.
- [2] J. Rösler, "Zur Tragfähigkeitssteigerung thermoplastischer Zahnräder mit Füllstoffen," Dissertation, Berlin, Germany, 2005.
- [3] M. Berer and Z. Major, "Characterization of the global deformation behaviour of engineering plastics rolls," *International Journal of Mechanics and Materials in Design*, vol. 6, no. 1, pp. 1–9, 2010.
- [4] M. Berer and Z. Major, "Characterisation of the local deformation behaviour of engineering plastics rolls," *Strain*, vol. 48, no. 3, pp. 225–234, 2012.
- [5] S. Lüftl, P. M. Visakh, and S. Chandran, *Polyoxymethylene Handbook: Structure, Properties, Applications and Their Nanocomposites*, Wiley, New Jersey, NJ, USA, 2014.
- [6] F. Arbeiter, B. Schritteser, A. Frank, M. Berer, and G. Pinter, "Cyclic tests on cracked round bars as a quick tool to assess the long term behaviour of thermoplastics and elastomers," *Polymer Testing*, vol. 45, pp. 83–92, 2015.
- [7] P. Schrader, A. Gosch, M. Berer, and S. Marzi, "Fracture of thin-walled polyoxymethylene bulk specimens in modes I and III," *Materials (Basel, Switzerland)*, vol. 13, 2020.
- [8] M. Berer, G. Pinter, and M. J. Feuchter, "Fracture mechanical analysis of two commercial polyoxymethylene homopolymer resins," *Applied Polymer Science*, vol. 131, p. 40831, 2014.
- [9] M. Berer, M. Halb, M. Feuchter, G. Pacher, and G. Pinter, "Fatigue fracture properties and morphology of polyoxymethylene (POM) plates produced under moderate processing conditions," *International Journal of Polymer Science*, vol. 2018, pp. 1–18, 2018.
- [10] A. Gosch, M. Berer, P. Hutař et al., "Mixed Mode I/III fatigue fracture characterization of Polyoxymethylene," *International Journal of Fatigue*, vol. 130, p. 105269, 2020.
- [11] R. Greco and G. Ragosta, "Isotactic polypropylenes of different molecular characteristics: influence of crystallization conditions and annealing on the fracture behaviour," *Journal of Materials Science*, vol. 23, no. 11, pp. 4171–4180, 1988.
- [12] G. Kalay and M. J. Bevis, *Polypropylene: An A-Z Reference*, J Karger-Kocsis, Ed., pp. 329–334, Springer, Dordrecht, Netherlands, 2012.
- [13] D. G. M. Wright, R. Dunk, d. Bouvart, and M. Autran, "The effect of crystallinity on the properties of injection moulded polypropylene and polyacetal," *Polymer*, vol. 29, no. 5, pp. 793–796, 1988.
- [14] R. Čermák, M. Obadal, P. Ponižil, M. Polášková, K. Stoklasa, and A. Lengálová, *European Polymer Journal*, vol. 41, pp. 1838–1845, 2005.
- [15] G. r. Kalay and M. J. Bevis, "Processing and physical property relationships in injection-molded isotactic polypropylene. 1. mechanical properties," *Journal of Polymer Science Part B: Polymer Physics*, vol. 35, no. 2, pp. 241–263, 1997.
- [16] J. Runt and K. P. Gallagher, "The influence of microstructure on fatigue crack propagation in polyoxymethylene," *Journal of Materials Science*, vol. 26, no. 3, pp. 792–798, 1991.
- [17] C. J. G. Plummer, P. Menu, N. Cudré-Mauroux, and H.-H. Kausch.
- [18] C. J. G. Plummer, P. Béguelin, and H.-H. Kausch, "The temperature and strain-rate dependence of mechanical properties in polyoxymethylene," *Polymer Engineering & Science*, vol. 35, no. 16, pp. 1300–1312, 1995.
- [19] J. C. Viana, "The local thermomechanical conditions and the fracture behavior of an injection-molded poly(oxymethylene)," *Polymer Engineering & Science*, vol. 46, no. 2, pp. 181–187, 2006.
- [20] X. Zhao and L. Ye, "Structure and properties of highly oriented polyoxymethylene produced by hot stretching," *Materials Science and Engineering: A*, vol. 528, no. 13–14, pp. 4585–4591, 2011.
- [21] S. T. Saravanan, C. Kailasanathan, E. Natarajan, and A. Ramasamy, "Crystallinity change and reduced warpages on thin walled parts—the effect of nano fumed silica on polyacetal," *Silicon*, vol. 13, no. 12, pp. 4611–4622, 2021.
- [22] C. K. Kailasanathan, S. T. Saravanan, E. Natarajan, and B. Stalin, "Polyoxymethylene/talc composite: investigation of warpage, mechanical and thermal properties for thin walled-injection molding applications," *Journal of Applied Polymer Science*, vol. 139, no. 10, p. 51762, 2022.
- [23] M. D. Azaman, S. M. Sapuan, S. Sulaiman, E. S. Zainudin, and A. Khalina, "Numerical simulation analysis of the in-cavity residual stress distribution of lignocellulosic (wood) polymer composites used in shallow thin-walled parts formed by the injection moulding process," *Materials & Design*, vol. 55, pp. 381–386, 2014.
- [24] D. A. de Miranda and A. L. Nogueira, "Simulation of an injection process using a cae tool: assessment of operational conditions and mold design on the process efficiency," *Mathematical Research*, vol. 22, 2019.
- [25] W. M. Ghazali, D. M. N. D. Idris, A. H. Sofian, J. P. Siregar, and M. F. Basrawi, "Gate location and injection analysis of a spur gear," in *Proceedings of the MATEC Web Conference*, p. 6012, Phuket, Thailand, July 2018.
- [26] Y.-K. Yang, J.-R. Shie, H.-T. Liao, J.-L. Wen, and R.-T. Yang, "A study of taguchi and design of experiments method in injection molding process for polypropylene components," *Journal of Reinforced Plastics and Composites*, vol. 27, no. 8, pp. 819–834, 2008.
- [27] C.-P. Chen, M.-T. Chuang, Y.-H. Hsiao, Y.-K. Yang, and C.-H. Tsai, "Simulation and experimental study in determining injection molding process parameters for thin-shell plastic parts via design of experiments analysis," *Expert Systems with Applications*, vol. 36, no. 7, pp. 10752–10759, 2009.
- [28] S. Rajalingam, A. Bono, and J. Bin Sulaiman, *Sri Lankan Journal of Application Statistics*, vol. 12, 2012.
- [29] S. Kleindel, R. Eder, H. Schretter, and C. Hochenauer, "Experimental and numerical investigation of shrinkage and warpage of a U-shaped injection molded part," *International Polymer Processing*, vol. 31, no. 1, pp. 68–81, 2016.
- [30] K. K. Kabanemi, H. Vaillancourt, H. Wang, and G. Salloum, "Residual stresses, shrinkage, and warpage of complex injection molded products: numerical simulation and experimental validation," *Polymer Engineering & Science*, vol. 38, no. 1, pp. 21–37, 1998.
- [31] X. Li, J. Ouyang, and W. Zhou, *CMES-Computer Modeling in Engineering & Sciences*, pp. 379–407, 2013.
- [32] A. Östergren, "Prediction of residual stresses in injection moulded parts Master's Thesis in the Applied Mechanics," Master's Thesis, Göteborg, Sweden, 2013.
- [33] C. Vargas, J. Sierra, J. Posada, and J. F. Botero-Cadavid, *Matéria. Revista Internacional d'Art*, vol. 22, p. 490, 2017.
- [34] T. J. Bress and D. R. Dowling, "Simulations and measurements of in-mold melt flow during the injection molding of

- polystyrene," *Polymer Engineering & Science*, vol. 53, no. 4, pp. 770–779, 2013.
- [35] P. Guerrier, G. Tosello, and J. H. Hattel, *Analysis of Cavity Pressure and Warpage of Polyoxymethylene Thin Walled Injection Molded Parts: Experiments and Simulations* AIP Publishing LLC, New York, NY, USA, 2015.
- [36] P. Guerrier, G. Tosello, and J. H. Hattel, "Flow visualization and simulation of the filling process during injection molding," *CIRP Journal of Manufacturing Science and Technology*, vol. 16, pp. 12–20, 2017.
- [37] U. Vietri, A. Sorrentino, V. Speranza, and R. Pantani, "Improving the predictions of injection molding simulation software," *Polymer Engineering & Science*, vol. 51, no. 12, pp. 2542–2551, 2011.
- [38] V. Speranza, S. Liparoti, R. Pantani, and G. Titomanlio, *AIP Conference Proceedings*, vol. 1914, p. 160001, 2017.
- [39] M. R. Kamal, J. Chu, S. Derdouri, and A. Hrymak, "Morphology of microinjection moulded polyoxymethylene," *Plastics, Rubber and Composites*, vol. 39, no. 7, pp. 332–341, 2013.
- [40] C. Tan, S. Bai, and Q. J. Wang, *Applied Polymer Science*, vol. 131, 2014.
- [41] I. Coccorullo, R. Pantani, and G. Titomanlio, "Crystallization kinetics and solidified structure in iPP under high cooling rates," *Polymer*, vol. 44, no. 1, pp. 307–318, 2003.
- [42] W. J. Yoon, H. S. Myung, B. C. Kim, and S. S. Im, "Effect of shearing on crystallization behavior of poly(ethylene naphthalate)," *Polymer*, vol. 41, no. 13, pp. 4933–4942, 2000.
- [43] I. Coccorullo, R. Pantani, and G. Titomanlio, "Spherulitic nucleation and growth rates in an iPP under continuous shear flow," *Macromolecules*, vol. 41, no. 23, pp. 9214–9223, 2008.
- [44] R. Pantani, F. de Santis, V. Speranza, and G. Titomanlio, "Modeling morphology evolution during injection molding of thermoplastic polymers," in *Proceedings of the PPS-30: The 30th International Conference of the Polymer Processing Society – Conference Papers*, p. 50006, June 2015.
- [45] R. Pantani, F. De Santis, V. Speranza, and G. Titomanlio, "Analysis of flow induced crystallization through molecular stretch," *Polymer*, vol. 105, pp. 187–194, 2016.
- [46] S. Cheng, L. Johnson, and S.-Q. Wang, "Crazing and strain localization of polycarbonate glass in creep," *Polymer*, vol. 54, no. 13, pp. 3363–3369, 2013.
- [47] Y. Wang, W. Zhao, X. Wang, and D. Wu, "Preparation, mechanical properties and microstructure of polyoxymethylene fiber through melt spinning and hot drawing by using injection-molding grade resins," *Fibers and Polymers*, vol. 17, no. 9, pp. 1464–1474, 2016.
- [48] R. Pantani, F. de Santis, V. Speranza, and G. Titomanlio, Eds., in *Proceedings of the 29th International Conference of the Polymer Processing Society-- Conference Papers* AIP Publishing, Melville New York, July 2013.
- [49] S. Liparoti, V. Speranza, R. Pantani, and G. Titomanlio, *Materials (Basel, Switzerland)*, vol. 12, 2019.
- [50] E. Andreasson, L. Persson, H. Jacobsson, and J. Nordgren, *SIMULIA Community Conference*, 2013.
- [51] X. Li, Q. Wei, J. Li et al., *Journal of Polymer Research*, vol. 26, 2019.
- [52] R. Pantani, I. Coccorullo, V. Speranza, and G. Titomanlio, "Modeling of morphology evolution in the injection molding process of thermoplastic polymers," *Progress in Polymer Science*, vol. 30, no. 12, pp. 1185–1222, 2005.
- [53] R. Pantani, I. Coccorullo, V. Speranza, and G. Titomanlio, "Morphology evolution during injection molding: effect of packing pressure," *Polymer*, vol. 48, no. 9, pp. 2778–2790, 2007.
- [54] S. Liparoti, V. Speranza, G. Titomanlio, and R. Pantani, *Polymers*, vol. 12, 2020.
- [55] S. Liparoti, A. Sorrentino, and V. Speranza, *Polymers*, p. 13, 2021.
- [56] AUTODESK Help, *Moldflow Insight: Theoretical Basis for Crystallization Analysis*, 2018.
- [57] J. I. Lauritzen and J. D. Hoffman, "Theory of formation of polymer crystals with folded chains in dilute solution," *Journal of Research of the National Bureau of Standards Section A: Physics and Chemistry*, vol. 64A, no. 1, pp. 73–102, 1960.
- [58] J. D. Hoffman and R. L. Miller, "Kinetic of crystallization from the melt and chain folding in polyethylene fractions revisited: theory and experiment," *Polymer*, vol. 38, no. 13, pp. 3151–3212, 1997.
- [59] R. Zheng and P. K. Kennedy, "A model for post-flow induced crystallization: general equations and predictions," *Journal of Rheology*, vol. 48, no. 4, pp. 823–842, 2004.
- [60] I. M. Krieger and T. J. Dougherty, "A mechanism for non-Newtonian flow in suspensions of rigid spheres," *Transactions of the Society of Rheology*, vol. 3, no. 1, pp. 137–152, 1959.
- [61] R. Pantani, V. Speranza, and G. Titomanlio, "Effect of flow-induced crystallization on the distribution of spherulite dimensions along cross section of injection molded parts," *European Polymer Journal*, vol. 97, pp. 220–229, 2017.
- [62] S. Liparoti, A. Sorrentino, G. Guzman, M. Cakmak, and G. Titomanlio, "Fast mold surface temperature evolution: relevance of asymmetric surface heating for morphology of iPP molded samples," *RSC Advances*, vol. 5, no. 46, pp. 36434–36448, 2015.